Acta Materialia 201 (2020) 182–190

Contents lists available at ScienceDirect

Acta Materialia

journal homepage: www.elsevier.com/locate/actamat

Full length article

Machine learning-based glass formation prediction in multicomponent alloys

Xiaodi Liu[a], Xin Li[a], Quanfeng He[b], Dandan Liang[a,c], Ziqing Zhou[b], Jiang Ma[a], Yong Yang[b,d], Jun Shen[a,*]

[a] College of Mechatronics and Control Engineering, Shenzhen University, Shenzhen 518060, China
[b] Department of Mechanical Engineering, College of Engineering, City University of Hong Kong, Kowloon Tong, Kowloon, Hong Kong SAR, China
[c] Key Laboratory of Optoelectronic Devices and Systems of Ministry of Education and Guangdong Province, College of Optoelectronic Engineering, Shenzhen University, Shenzhen 518060, China
[d] Department of Materials Science and Engineering, College of Engineering, City University of Hong Kong, Kowloon Tong, Kowloon, Hong Kong SAR, China

ARTICLE INFO

Article history:
Received 21 June 2020
Revised 2 September 2020
Accepted 25 September 2020
Available online 4 October 2020

Keywords:
Metallic glasses
Glass-forming ability
Machine learning

ABSTRACT

Metallic glasses (MGs) have attracted considerable academic attention owing to their unique properties and great application prospects. Unlike other glassy materials, such as oxide glasses, MGs have limited glass forming-ability (GFA) that often leads to failure during new MG development. Although intensive studies have proposed various parameters and criteria enabling the evaluation of the GFA of MG samples, achieving accurate predictions of glass formation before the actual MG sample synthesis remains a great challenge and an open topic. In this study, we investigated the glass formation through the data-driven machine learning technique and trained a backpropagation neural network model based on a dataset assembled from thousands of ternary alloys. Applying the well-trained model, we accurately identified the MG and non-MG classes. More importantly, our model can effectively predict glass-formation likelihood of multicomponent alloys and locate the probable MG compositions without any prior experiment, thereby directing the MG design. From the model's predictions, we discovered several new MGs in the ribbon form. Glass-formation likelihood reveals the correlation with the thermodynamic and topological parameters, which provides insights into the GFA of MGs.

1. Introduction

Metallic glasses (MGs) have a nonequilibrium nature [1] but do not have long-range translational symmetry in atomic arrangement [2], hence possessing various unique properties, such as high strength, high elastic limit, and superb corrosion resistance [3,4]. Since Duwez et al. first synthesized MGs by quenching in 1960 [5], thousands of glass-formers in diverse alloy systems have been constantly discovered through the rapid solidification method. However, compared with inorganic and polymeric glasses, MGs have an extremely limited glass-forming ability (GFA, i.e. the ability of a material to transform into a glassy state [6]), which often incurs the development failure of new MGs. To design MGs in a reasonable, reliable and reproducible way, it is essential to understand the fundamental physics of glass formation from supercooled liquids. Thermodynamically, the small driving force of crystallization favoring MG formation requires small enthalpy and large entropy of fusion. These requirements can be achieved by increasing the number of components and creating dense atomic packing by introducing a large atomic size difference [7], in consistent with Greer's confusion principle [8], Hume-Rothery's criterion [9] and Inoue's criteria [10]. The near deep eutectic compositions promote MG formation because the decreased melting temperature stabilizes the disordered liquid state, and the competition between multiple crystalline phases and the disordered liquid phase suppresses the nucleation [6]. Furthermore, MG formation is kinetically preferred as the nucleation rate is suppressed by increasing the liquid–crystal interface energy and reducing the long-range atomic diffusion, which show the association with the high thermodynamic interface penalty [11], the high fragility of liquids [12–15], and the dense atomic packing of the multiple components [10]. From the structural perspective, the enhanced atomic size mismatch induces a high internal strain [16–18], leading to lattice distortion and instability [7,9]. The presence of short-to-medium range orders, such as hidden topological orders [19], spherical-periodic orders, and local translational symmetry [20], also chemically and topologically stabilizes the disordered structures. To date,

* Corresponding author.
E-mail address: junshen@szu.edu.cn (J. Shen).

https://doi.org/10.1016/j.actamat.2020.09.081
1359-6454/

identifying the key physical factor for vitrification is still an open topic under intensifying debate.

On the basis of the physical understanding of the glass formation of MGs, extensive research has made great efforts for the feasible parameters or criteria of evaluating and predicting the GFA to satiate the burning desire for discovering new MGs. These parameters and criteria can be broadly grouped into the following categories [21], which depend on (i) characteristic transformation temperatures, such as reduced glass transition temperature ($T_{rg} = T_g/T_l$, where T_g is glass transition temperature and T_l is liquidus temperature) [22], ΔT_x parameter ($\Delta T_x = T_x - T_g$, where T_x is onset crystallization temperature) [23], γ parameter [$\gamma = T_x/(T_g + T_l)$] [24], γ_m parameter [$\gamma_m = (2T_x - T_g/T_l]$ [25], (ii) thermodynamic quantities, such as the enthalpy of mixing (ΔH_{mix}) [10], the enthalpy of formation of solid solution (ΔH_{ss}) [26], (iii) topological and structural features, such as configurational entropy (ΔS_c) [27], mismatch entropy (S_σ) [28], atomic size difference (δ) [10], Pauling's electronegativity difference ($\Delta\chi$) [29] and valence electron concentration (*VEC*) [30], and (iv) kinetic properties, such as fragility (m) [31,32]. Although these parameters and criteria reveal the interpretation of glass formation from distinct points of view, they are not universally valid for the entire MG family. Moreover, most of these parameters rely on experimental measurements on actual MG samples and consequently lack the predictability of glass formation. Evidently, such parameters are inconvenient to guide MG design. When we develop new MGs on the basis of these parameters and criteria, large numbers of trial-and-error experiments are necessary, which are time consuming and resource-intensive [33].

A novel paradigm based on machine learning (ML) techniques is emerging for materials science; it shows potential in glass-formation prediction and the acceleration of discovering new MGs [33,34]. Such a data-driven approach enables rapid estimations based purely on past data without any additional experimentations and simulations [35]. Accordingly, we can get rid of the conventional trial-and-error experiments. Applying a variety of ML algorithms, such as neural network [36–41], support vector machine [42], random forest [43–45], decision trees [46], support vector regression [47] and Gaussian process [47], the ML models realize the assessment of R_c [36,39], d_{max} [44,47], T_g [36,40], T_{rg} [37] and ΔT_x [38] and propose new predictive criteria for binary [42], ternary [43] and multicomponent alloys [41].

In this study, we intend to investigate the glass formation of MGs through training a backpropagation neural network (BPNN) model based on a dataset assembled from thousands of ternary alloys. Through the ingenious approximations of features that we select, we tackle the problem that several features, such as ΔT_x, are unobtainable without prior experiments on actual MG samples, and thus realize taking the thermodynamic, kinetic, and structural aspects into considerations within one predictive model, which has not been achieved before. We aim to identify MG and non-MG classes accurately by applying our well-trained model. More importantly, the model can be used to predict the glass formation of MGs and locate the probable MG compositions without any prior synthesis and measurement, thereby effectively guiding the MG design.

2. Methods

2.1. Data collection and processing

The data were collected from the handbook "Phase diagrams of non-equilibrium alloys" [48]. The dataset consists of 3,227 compositions in 79 ternary alloy systems, containing 31 metals and 2 metalloids. A total of 1,850 MG compositions, 908 crystalline compositions, and 469 mixed ones exist in the dataset, accounting for 57%, 28% and 15%, respectively. To train the model, we categorized the data on the basis of their structures, forming a MG class and a non-MG class that combines the crystalline data with the mixed data. The imbalanced data (i.e. the MG class vs. the non-MG class is 57% to 43%) are likely to degrade the training performance of the classifier systematically. Therefore, we performed a random undersampling test with the synthetic training data. The result shows no discrepancy of performance between the resampled and raw datasets (Appendix A); thus, we accepted this slightly skewed dataset to avert the risk of overfitting or information loss from resampling. The dataset was randomly divided into three subsets, including a training dataset (accounting for 70%), a validation dataset (15%) and a test dataset (15%).

2.2. Feature calculation and selection

According to the extensive studies on the GFA of MGs [10,22–25,28–30,49–58], we initially selected 23 parameters as feature candidates, which were either physical quantities or artificial parameters proved relevant to GFA. To achieve the predictability of glass formation, it is of crucial importance that the acquirement of features must not rely on any sample synthesis and measurement. Therefore, every feature that we selected was obtained by theoretical calculation or approximation, as listed in Table 1.

In order to reduce overfitting and prevent the curse of dimensionality, we applied a two-step filter method to remove redundant and low-variance features. First, we analyzed the linear correlation among all feature candidates by calculating the Pearson's correlation coefficient ($\rho_{A,B}$) of each pair of features (*A*,*B*), which is given by the equation: $\rho_{A,B} = E[(A - \mu_A)(B - \mu_B)]/(\sigma_A\sigma_B)$, where E[•] is the expectation; μ_A and μ_B are the means of *A* and *B*, respectively; and σ_A and σ_B are the standard deviations. $\rho_{A,B}$ ranges from −1 to 1; its value is equal to 1, −1 and 0, denoting perfectly positive, negative and no correlation, respectively. The redundant features with strong correlation ($\rho_{A,B} < -0.7$ or > 0.7) were highlighted in Fig. 1, on the basis of the correlation matrix. We observed that there are four strong correlated parameter pairs, i.e. ΔT_x – ω, T_l – ω, T_x – V and K – V, and two strong correlated parameter groups, i.e. (T_g, E, G, K, T_l, T_x) and (T_{rg}, ω, γ, α, β, γ_m, ξ). It is necessary

Table 1
Formulae of feature candidate calculation

Feature candidates	Formulae
Pauling's electronegativity difference [29]	$\Delta\chi = \sqrt{\sum_{i=1}^{n} c_i(\chi_i - \chi)^2}$
Valence electron concentration [30]	$VEC = \sum_{i=1}^{n} c_i(VEC)_i$
Theoretical density [49]	$\rho = 100/(\sum_{i=1}^{n} W_i/\rho_i)$
Theoretical molar volume [50]	$V = \sum_{i=1}^{n} c_i m_i/\rho_i$
Atomic size difference [10]	$\delta = \sqrt{\sum_{i=1}^{n} c_i(1 - r_i/\bar{r})^2}$
Enthalpy of mixing [10,51]	$\Delta H_{mix} = \sum_{i=1, j\neq i}^{n} \Omega_{ij} c_i c_j$
Configurational entropy [52]	$\Delta S_c = -R\sum_{i=1}^{n} c_i \ln c_i$
Mismatch entropy [28,49]	$S_\sigma = k_B\{1.5(\zeta^2 - 1)y_1 + 1.5(\zeta - 1)^2 y_2 - [0.5(\zeta - 1)(\zeta - 3) + \ln\zeta](1 - y_3)\}$
Modulus [50,53,54]	$M_{hi} = \sum_{i=1}^{n} c_i M_i V_i/V$ (upper bound) $M_{lo} = V/(\sum_{i=1}^{n} c_i W_i/M_i)$ (lower bound)
Fragility [55]	$m = 12(K/G + 0.67)$
Glass transition temperature [50]	$T_g = 2.5E + C_1$
Melting temperature [50]	$T_l = VE/C_2R$
Onset crystallization temperature [50]	$T_x = C_3K + C_4$
T_{rg} parameter [22]	$T_{rg} = T_g/T_l$
ΔT_x parameter [23]	$\Delta T_x = T_x - T_g$
α parameter [56]	$\alpha = T_x/T_l$
β parameter [56]	$\beta = (T_x/T_g) + (T_g/T_l)$
γ parameter [24]	$\gamma = T_x/(T_g + T_l)$
γ_m parameter [25]	$\gamma_m = (2T_x - T_g)/T_l$
ξ parameter [57]	$\xi = T_g/T_l + \Delta T_x/T_x$
ω parameter [58]	$\omega = T_g/T_x - 2T_g/(T_g + T_l)$

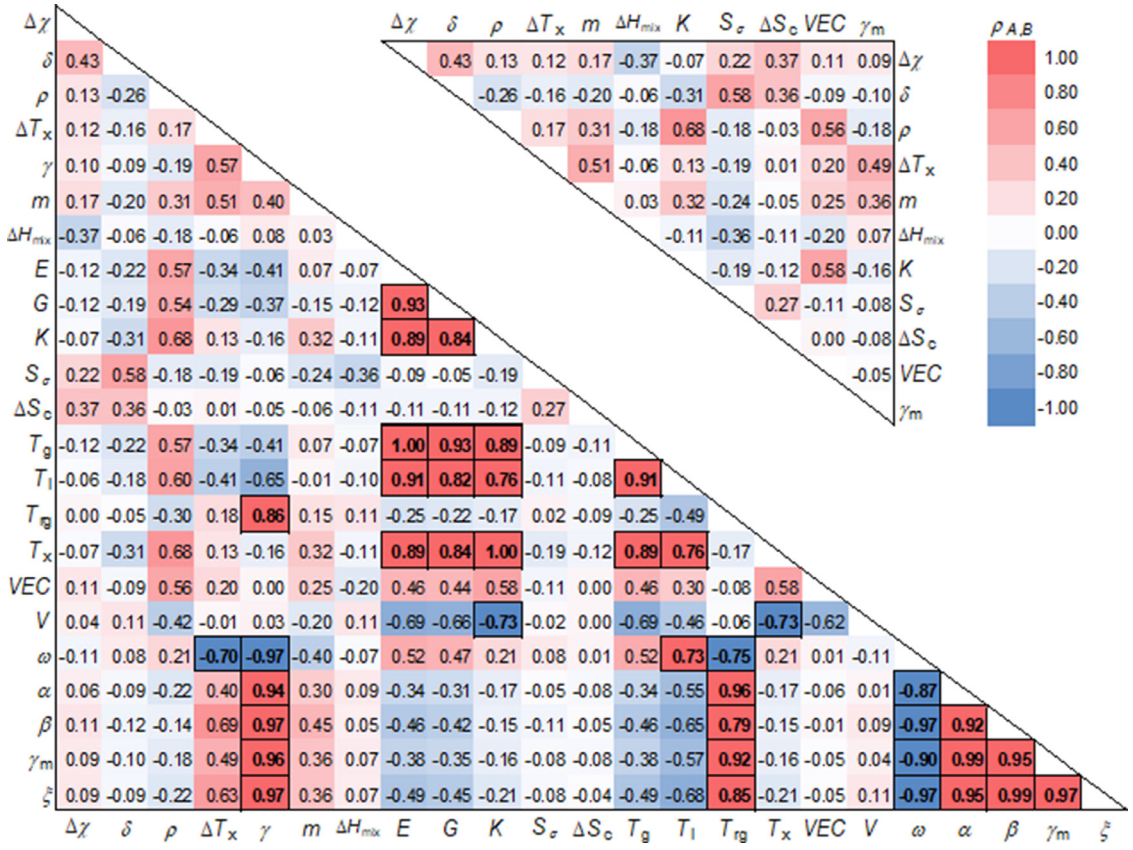

Fig. 1. Correlation matrices with heatmaps. Due to the reflectional symmetry along the main diagonal, half of the bits in the matrices are not presented. The lower matrix displays the correlation coefficient of all feature candidates, while the upper one shows the results after the two-step feature filtration.

to select only one and rule out other parameters within the same pair/group for ML model training.

Second, the features were filtered on the basis of their dispersion. We calculated the coefficient of variation c_v ($c_v = \sigma_A/|\mu_A| \times 100\%$), as shown in Fig. 2, which is a dimensionless number measuring the relative deviation from the mean μ_A. If c_v equals 0, then the feature is invariable. A qualified feature for ML model training should have a sufficiently high c_v, which indicates that the feature is widely distributed over a relatively large range, thereby characterizing different classes. Consequently, we deleted the low-variance features with $c_v < 30\%$ and selected the features with the highest c_v from the strong correlated pairs/groups. In other words, we removed T_g, E, G, T_l, T_x, T_{rg}, ω, γ, α, β, ξ, and V.

After applying the two-step filter method, we finally selected 11 features for our ML model training, i.e. Pauling's electronegativity difference ($\Delta\chi$), atomic size difference (δ), theoretical density (ρ), parameter ΔT_x, parameter γ_m, fragility (m), enthalpy of mixing (ΔH_{mix}), mismatch entropy (S_σ), configurational entropy (ΔS_c), bulk modulus (K), and valence electron concentration (VEC). These features are the descriptors of alloys from the perspective of thermodynamics, kinetics, and structures. They can be transformed into a feature vector, having a one-to-one correspondence to the alloy composition and class label (i.e. MG or non-MG).

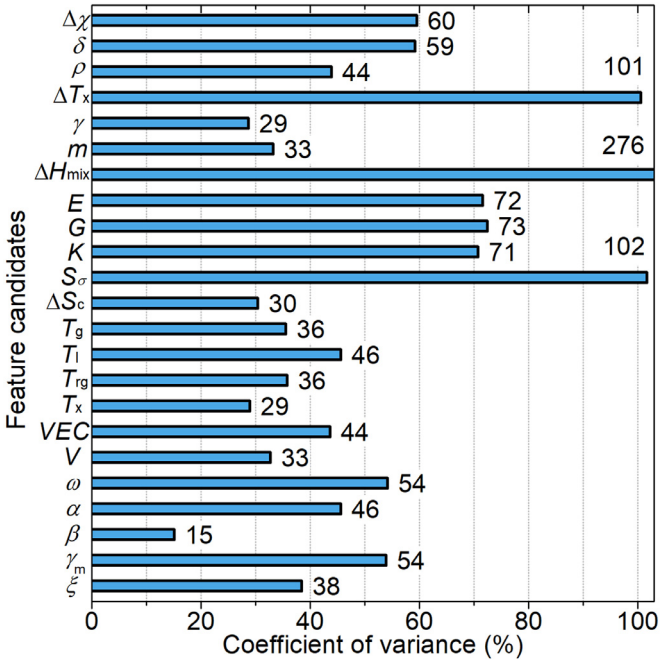

Fig. 2. Coefficient of variance of feature candidates.

2.3. Implementation of BPNN model

We employed an artificial neural network model with back-propagation learning algorithm [59], as illustrated in Fig. 3, which included an input layer receiving the features, a hidden layer with 22 neurons, and an output layer producing the results. The number of hidden neurons was determined through a 10-fold cross-validation technique, as discussed in Appendix B. During the feedforward computation, the hidden neurons processed the information from the input layer through a hyperbolic tangent transfer function $f(\mathbf{h}) = 2/[1 + \exp(-2\mathbf{h})] - 1$, where $\mathbf{h}$ is a vector

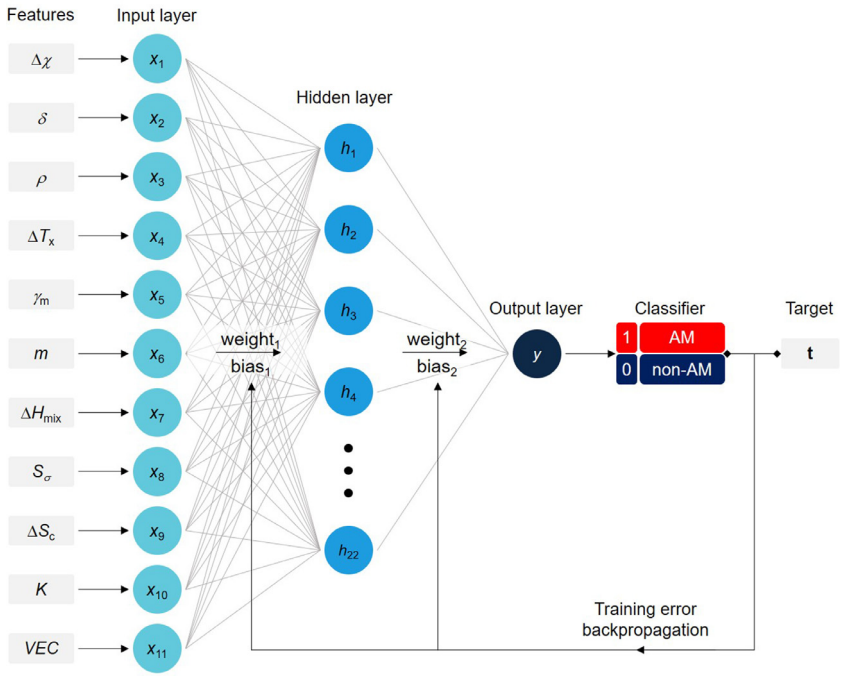

Fig. 3. Schematic of the BPNN model. The messages pass between the neurons in different layers in a one-way method through the adjustable weights and biases. The error between the output and the target class propagates backward to update the weights and biases thereby minimizing the global error and optimizing the model.

with the expression $\mathbf{h} = \mathbf{w}_1\mathbf{x} + \mathbf{b}_1$, $\mathbf{w_1}$ is the weight matrix, $\mathbf{x}$ is the input vector, and $\mathbf{b}_1$ is the bias vector. Similarly, the output neuron received the messages transmitted from the hidden layer and generated the output $\mathbf{y}$, as expressed by $\mathbf{y} = \mathbf{w}_2\mathbf{h} + \mathbf{b}_2$. In the classifier, $\mathbf{y}$ was rounded up to 1 or 0, corresponding to MG or non-MG class. We adopted the mean squared normalized error function to estimate the training error between $\mathbf{y}$ and the supervisory target $\mathbf{t}$. The training error was backward propagated for updating parameters $\mathbf{w}_1$, $\mathbf{w}_2$, $\mathbf{b}_1$, and $\mathbf{b}_2$ according to the Broyden–Fletcher–Goldfarb–Shanno (BFGS) algorithm. When the error converged to the minimum (actually oscillated around the minimum) [60], the iterative learning was completed. As a result, we obtained a well-trained BPNN model. The model was trained on the basis of MATLAB software. The dataset and input files necessary for reproduction are available on GitHub (https://github.com/xdliu-yahya/-BPNN_Glass_Formation).

2.4. Sample preparation and structure characterization

We used raw materials with purity > 99.9% in wt.% to prepare ingots by arc-melting under a Ti-gathered Ar atmosphere. Subsequently, the ingots were remelted through induction melting in a quartz tube under Ar atmosphere. The melts were ejected onto a single Cu roller with a surface speed of approximately 30 m/s to fabricate ribbons. The as-spun ribbons were approximately 3–5 mm in width and 30–50 μm in thickness. Thereafter, the ribbon samples were characterized by X-ray diffraction (XRD) by using Rigaku MiniFlex 600 with Cu Kα radiation at a scan rate of 4°/min. The compositions were determined using an energy dispersive X-ray (EDX) spectrometer attached to an FEI Quanta 450FEG scanning electron microscope instrument.

3. Results

3.1. Performance of BPNN model

Fig. 4a shows the confusion matrix of our well-trained BPNN model. On the basis of the predicted and actual classes, all data can be categorized as true positive (TP), true negative (TN), false positive (FP) and false negative (FN), with the number and percentage listed in Fig. 4a. To comprehensively assess the performance of our BPNN model, we analyzed a series of model evaluation metrics. Overall, the BPNN model can achieve correct predictions in 82.1% of cases. The accuracy (ACC) of 82.1% is acceptable, because an extremely high ACC may result from overfitting and insufficient test data. As shown in Fig. 4b, the learning curves of the model without high variance verify our model not overfitted. Fig. 4c presents that the average and standard deviation of ACC slightly changes from 78.9±3.3% to 77.8±1.2%, as the ratio of test to training set size grows. It is reasonable that we applied the ratio of ~0.18 (15% of data for test and others for training) thereby mediating the conflict of high deviation and ACC loss.

Furthermore, both precision and recall reveal the excellent validity of predicting a specific class by applying our model. The precision of the MG class (i.e. PPV = 81.6%) indicates that up to 81.6% of predictions on the MG class are correct, while the recall of the MG class (i.e. TPR = 88.8%) represents that our model can successfully identify 88.8% of actual MG compositions and miss only 11.2%. The capability of identifying the non-MG class is also important in our study, in which the precision (NPV) and recall (TNR) of the non-MG class are 82.9% and 73.1%, respectively. Precision and recall are usually two conflicting metrics, which means a model with improving precision often reduces recall and vice versa, as demonstrated in Fig. 4d. Evidently, our BPNN model at the threshold of ~0.6 (indicated by arrows) exhibits the optimum balance between precision and recall for the MG and non-MG classes due to the high F_1 score (where F_1 is the harmonic mean of precision and recall, as shown in Fig. 4e). It is worth emphasizing that we separately plotted the precision–recall curves of the training and test data, because the test data were not included in the training stage and able to verify the good generalization of our model. The results convincingly demonstrate that our BPNN model is extraordinarily robust to predict the glass formation of MGs.

We also analyzed the receiver operating characteristic (ROC) curves to judge the classification ability of our model. As shown in

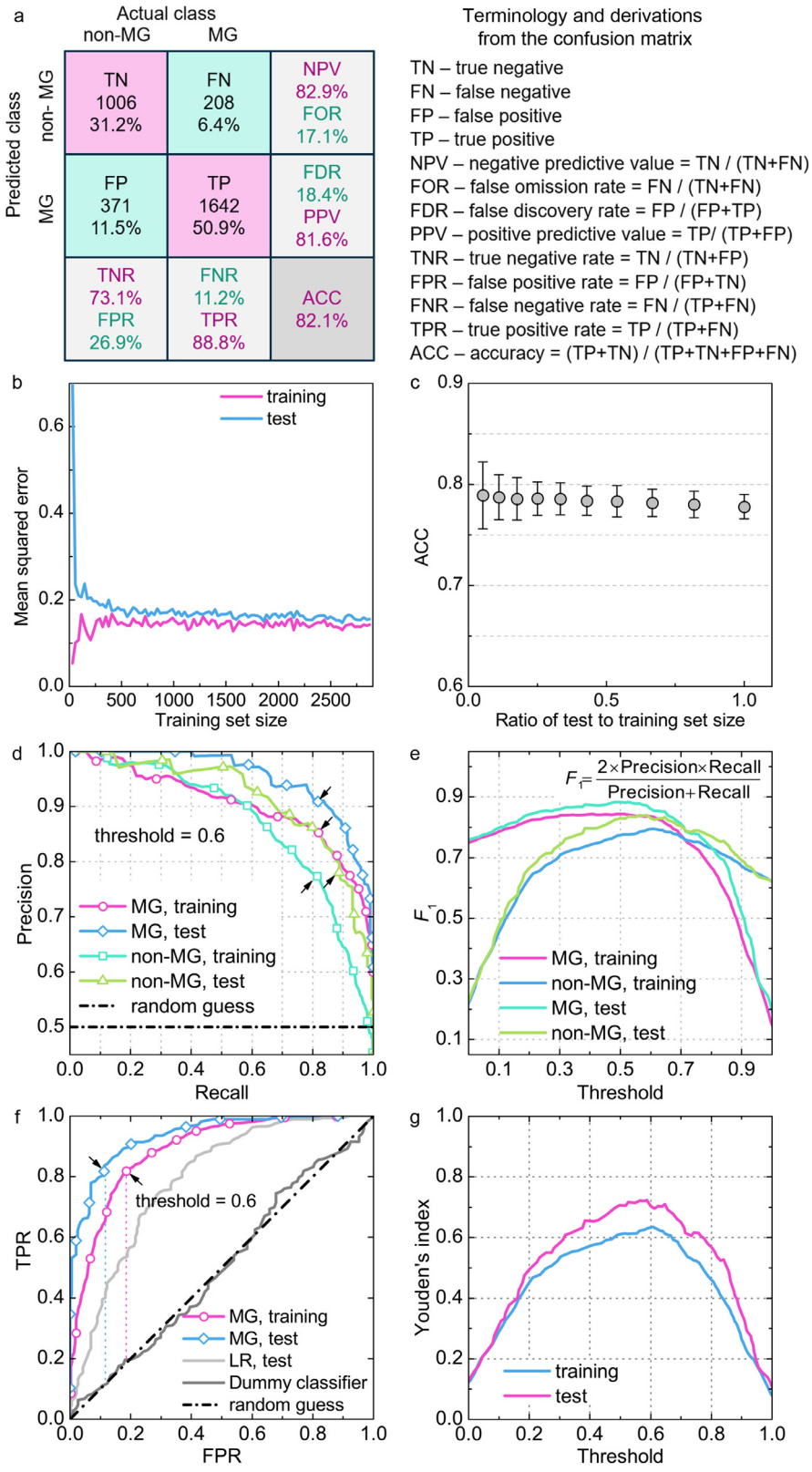

Fig. 4. Evaluation metrics of the BPNN model. (a) confusion matrix; (b) learning curves; (c) ACC variation with the ratio of test to training set size; (c) precision–recall curves; (f) F_1 score vs. threshold; (e) ROC curves; (f) Youden's index vs. threshold.

Fig. 4f, ROC curves plot the variations in TPR and FPR with changed thresholds. If a classifier has no classification capability, the ROC curve will comply with the random guess line, connecting points (0,0) and (1,1) with an area under the curve (AUC) of 0.5, such as the dummy classifier generating a baseline. For a skilled classifier, its ROC curve will bow toward the coordinate (0,1), which denotes the perfect classifier. For comparison purposes, we trained a logistic regression (LR) model, which is a linear classifier, equivalent to one neural node in neural networks. Evidently, the better performance of our BPNN model demonstrates the significance of using such a complex model (i.e. neural network). The curves at the threshold of ~0.6 have the optimized tradeoff of TPR and FPR due to the large Youden's index (i.e. the height above the chance line; details are presented in Fig. 4g). The AUC of 0.94 proves the excellent performance of the BPNN model in predicting glass formation. Compared with the curve of the training dataset, that of the test dataset does not show any deterioration, which confirms the good generalization of our model. Therefore, we can draw the conclusion that our BPNN model has extraordinary performance in evaluating and predicting the glass formation of MGs.

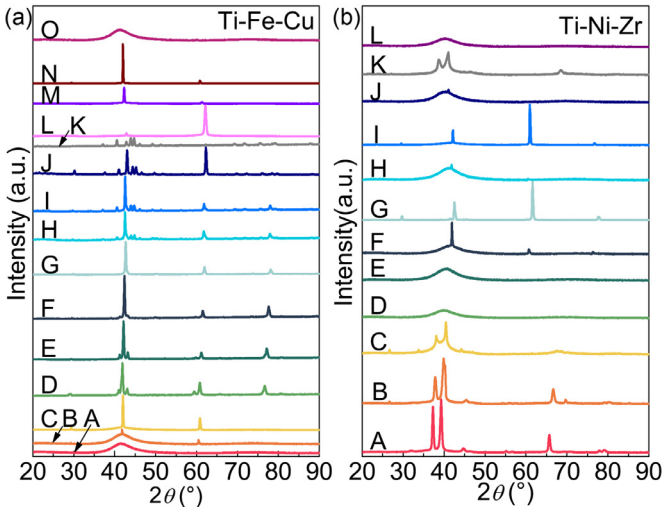

Fig. 6. XRD patterns of ribbon samples. (a) Ti-Fe-Cu system; (b) Ti-Ni-Zr system.

3.2. Prediction of glass-formation

We introduced the glass-formation likelihood (L), defined as the output value obtained from the BPNN model, which represents the confidence of the predictions for an alloy forming glassy state [43]. The compositions with high L are more likely to form a glassy state than the low-L ones under the same experimental conditions. Fig. 5 depicts four typical instances to illustrate this point. We applied our predictive model to four ternary alloy systems, i.e. Ti–Co–Zr, Fe–Co–Zr, Ti–Fe–Cu and Ti–Ni–Zr, and mapped the contours of L to visualize the probable glassy regions. In Figs. 5a and b, the lightened areas overlaying the color maps are MGs, whereas the darkened areas are not, as reported by Ren et al. [43] It is clear that the distribution of L matches with the experimental results in both ternary systems. Furthermore, Ti–Co–Zr and Fe–Co–Zr are the new alloy systems not included in the dataset, which confirms the remarkable predictability and generalization of our BPNN model.

Compared with the majority of GFA parameters and criteria, our BPNN model has the advantages of predicting the GFA of alloys ahead of actual sample preparation because it does not depend on experiments, such as the measurement of T_g, T_x, and T_l. Therefore, the BPNN model can guide MG design. To this end, we prepared some ribbons in Ti–Fe–Cu and Ti–Ni–Zr systems based on the L maps, as shown in Figs. 5c and d. The structures of the ribbons, characterized by XRD in Fig. 6, are plotted as symbols onto the contour maps of L. We observed that Ti–Fe–Cu has overall poor L but still has some relatively high-L values in narrow regions, in-

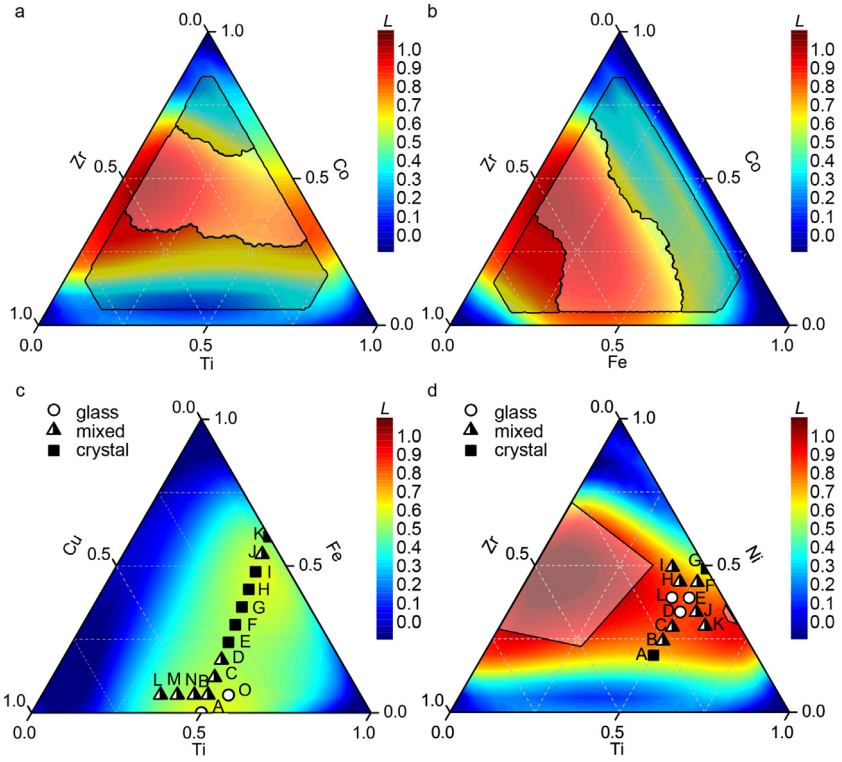

Fig. 5. Contour maps of L based on the predictions of the BPNN model. The lightened and darkened areas denote MGs and non-MGs reported in Ref. [43]. The scattered data are our experimental results. (a) Ti–Co–Zr system; (b) Fe–Co–Zr system; (c) Ti–Fe–Cu system; (d) Ti–Ni–Zr system.

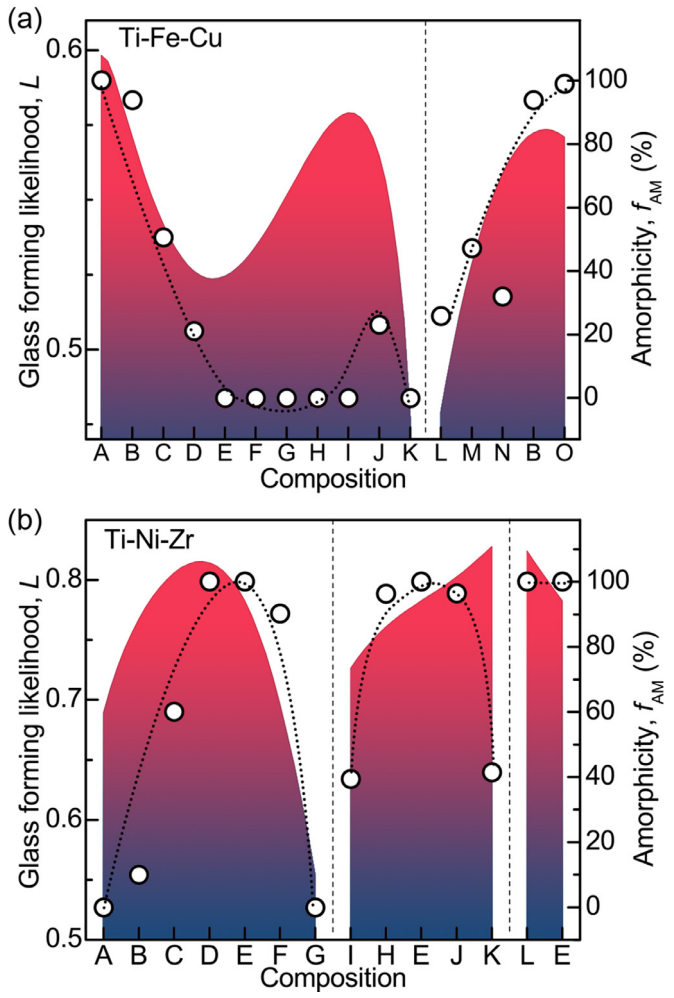

Fig. 7. Glass forming likelihood (filled curves) and amorphicity (scattered data). (a) Ti-Fe-Cu system; (b) Ti-Ni-Zr system.

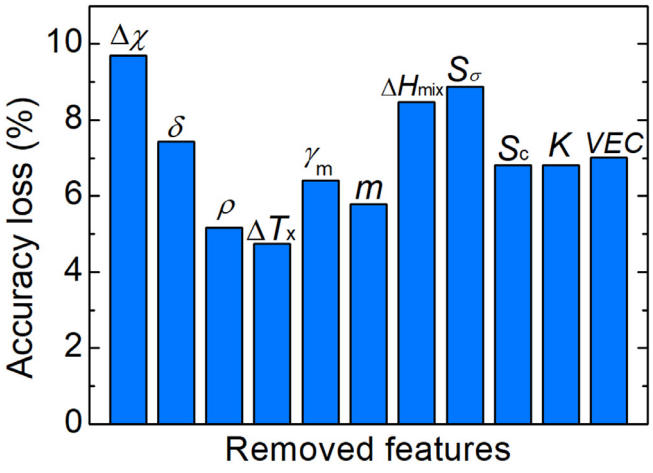

Fig. 8. Accuracy losses of the models with one feature removed during training.

dicating the potential MG compositions. Following the guide of L, we succeeded in developing two MGs from such an "unexpected" and "bad" glass formation alloys, which had not been reported before. Different from the easy task of fabricating MGs in the alloys with broad high-L areas, such as Ti–Co–Zr and Fe–Co–Zr, what we accomplished in Ti–Fe–Cu was a very difficult task, which demonstrates the outstanding ability to guide MG design. Another example that we chose was the Ti–Ni–Zr system. It provided the model some MG data for training, as presented by the lightened areas in Fig. 5d, and hence the highest-L regions matched these areas. We noticed that there were also some high-L compositions outside of these highest-L areas. Therefore, we intended to verify whether MGs can form in these "neglected" areas. Evidently, we discovered three full and several partial glassy structures in relatively large L regions, in line with the model's predictions. Here, we introduced amorphicity (f_{am}), which is the fraction of non-crystalline structures [$f_{am} = (1 - f_{cry}) \times 100\%$, where f_{cry} is the crystallinity, namely the fraction of crystalline state]. We found that the variation in f_{am} is roughly consistent with L, as shown in Fig. 7. The results prove that the maps of L generated by our predictive BPNN model are the competitive guide that assists in developing new MGs. However, it is necessary to emphasize that L = ~0.5 cannot be regarded as the threshold to distinguish glasses from crystals as it works in the prior binary classifier, since MG formation not only depends on GFA but also relates to the processing condition. Therefore, we conclude that there is a greater probability to fabricate MGs with high-L compositions than low-L ones under the same experimental conditions.

4. Discussion

4.1. Physical understanding of L

To understand the significances of the features to L, we trained models leaving each feature out one by one. And then we tracked the ACC losses. As shown in Fig. 8, ACCs decrease by over 7% when $\Delta\chi$, δ, ΔH_{mix} and S_σ is removed, which indicates that these features play key roles in our model. In accord with the Inoue's rules [10] and the Hume-Rothery's rule [9], the large δ leads to dense atomic packing and increased liquid–solid interfacial energy [6], causing the reduce of free volume, the increase of viscosity of melt and the sluggish atomic diffusivity. For alloys, low $\Delta\chi$ promotes the formation of solid solutions [61], whereas high $\Delta\chi$ suggests relatively strong atomic interactions, i.e. the formation of clusters. Such atomic interactions can restrain the solubility and diffusion of these elements in the competing crystalline phases and thus stabilize liquid phases during cooling [29,61,62]. Topologically, large S_σ indicates an extreme mismatch in atomic sizes that induces large intrinsic residual strains and results in lattice instability favoring glass formation [16–18].

4.2. Generalization to multicomponent alloys

Although the whole data used for training the model were collected from the alloys containing three components ($n \leq 3$) at most, the well-learned model did not limit the number of components in physics. To generalize our model to multicomponent alloys ($n > 3$), we collected 386 multicomponent compositions from literature (Supplementary Table 1 presents the composition list) and then verified the model predictions with these data. As shown in Fig. 9, the histograms depict the probability density distributions of L of MG and non-MG alloys. Clearly, L exhibits the Gaussian distribution with the average value of 0.51 for non-MGs and 0.87 for MGs, indicating their difference in GFA can be distinguished by our model. The accuracy of predictions is 83% due to 17% of area overlapped in Fig. 9. As a consequence, we successfully generalized our BPNN model to acquire predictions of L of multicomponent alloys.

4.3. Prediction error

The prediction error of our BPNN model may result from the training data, feature obtainment, and model tradeoff. First, the

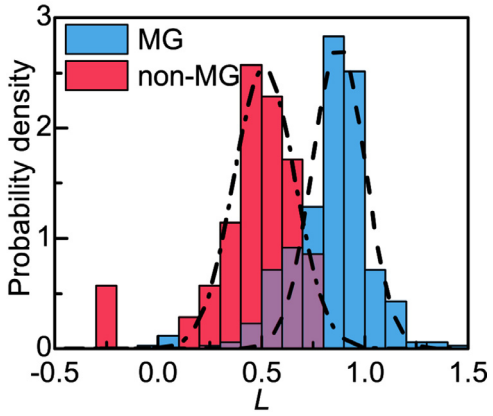

Fig. 9. Probability density distributions of *L* of MG and non-MG multicomponent alloys.

performance of a ML model strongly relies on the quantity and quality of data; therefore, collecting more typical data for training via data augmentation, data selection, and combination with high throughput observations [43] is an effective approach that further improves the model performance and generalization capability. Second, in order to achieve the predictability of glass formation and eliminate the dependence on the measurement of features, we applied the theoretical calculation and the mixing rule to estimate the features, which introduced a calculation error into the BPNN model. Instead of estimations with explicit expressions, we can expect that ML directly obtain the accurate values of features, such as moduli and characteristic temperatures [36–38,47,63,64]. Third, several inevitable dilemmas occur during model parameter determination, such as the tradeoff between model parsimony and performance accuracy, between precision and recall, and between TPR and FPR. The compromise will reduce overfitting and improve the generalization of the model.

5. Conclusion

In conclusion, we developed a ML model based on the BPNN algorithm and the data of ternary alloys in this study. Our BPNN model reveals extraordinary performance in identifying the MG and non-MG classes. To validate and generalize the BPNN model, we compared the predictions of the BPNN model with masses of experimental results reported in literature and conducted in this work. The results prove that our predictive model can evaluate and predict the glass-formation likelihood of alloys without any prior experiment. Therefore, it can be used for guiding MG design. From the predictions of the probable MG formation regions given by our model, we successfully discovered several new MG compositions in varied alloy systems.

Declaration of Competing Interest

None.

Acknowledgements

This work is supported by China National Natural Science Foundation (No. 52071217) and China National Key Research and Development Program (No. 2018YFA0703605). D.D.L. was supported by the NSFC [grant number 51901138]. Y.Y. was supported by Research Grants Council, the Hong Kong Government, through the General Research Fund (GRF) with the grant members City U11209317 and City U11213118.

Supplementary materials

Supplementary material associated with this article can be found, in the online version, at doi:10.1016/j.actamat.2020.09.081.

Appendix A. Undersampling test

There are 1,850 data of MG class and 1,377 data of non-MG class in the original training dataset. To create a balanced dataset, we randomly selected 1,377 samples from the MG class and combined with the whole of non-MG class. By comparison, 2,754 data were randomly extracted to form the imbalanced dataset as skewed as the original dataset. After training ML models by using these two datasets for 30 times respectively, we applied the mean squared error (MSE) to evaluate the performance of the ML models. The averaged MSE is 0.16 ± 0.01 for using the balanced data and 0.15 ± 0.01 for employing the biased one. Both have a low MSE that shows a good performance. Furthermore, there is nearly no difference between them, and the skewed data even perform a little better. Therefore, it demonstrates that a slightly imbalanced dataset in our training is acceptable, having little impact on the ML model performance.

Appendix B. Determination of number of hidden neurons

To determine the number of hidden neurons, we trained a series of ML models with the varying numbers from 1 to 100, through the 10-fold cross-validation method. Afterwards, we calculated the training errors and validation errors of these models, as shown in Fig. B.1. The training error gradually decreases with the increasing number of hidden neurons and then fluctuates between 0.13 to 0.15, which means the performance of ML model initially improves and subsequently remains nearly stable. Similar trend can be seen in the validation error, revealing a similar generalization accuracy for the unseen instances. Though there is no evident overfitting effect (i.e. training error reducing but validation error going up) in Fig. B.1, we decide to use a small number of hidden neurons to balance the model performance and complexity. Ultimately, we applied 22 hidden neurons in our model.

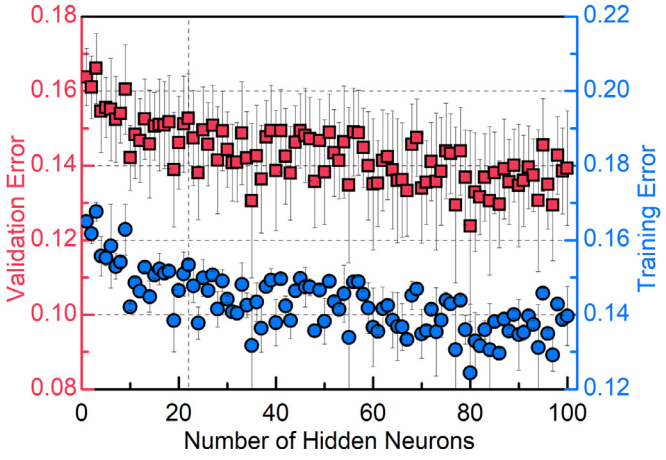

Fig. B.1. Validation and training error variation with the number of hidden neurons.

References

[1] E.D. Zanotto, J.C. Mauro, The glassy state of matter: its definition and ultimate fate, J. Non-Cryst. Solids 471 (2017) 490–495.
[2] H. Tanaka, T. Kawasaki, H. Shintani, K. Watanabe, Critical-like behaviour of glass-forming liquids, Nat. Mater. 9 (4) (2010) 324–331.
[3] C.A. Schuh, T.C. Hufnagel, U. Ramamurty, Mechanical behavior of amorphous alloys, Acta Mater. 55 (12) (2007) 4067–4109.
[4] M. Telford, The case for bulk metallic glass, Mater. Today 7 (3) (2004) 36–43.
[5] W. Klement Jun, R.H. Willens, P.O.L. Duwez, Non-crystalline structure in solidified gold–silicon alloys, Nature 187 (1960) 869.
[6] C. Suryanarayana, A. Inoue, Bulk Metallic Glasses, CRC press, Boca Raton, 2017.
[7] T. Egami, Y. Waseda, Atomic size effect on the formability of metallic glasses, J. Non-Cryst. Solids 64 (1) (1984) 113–134.
[8] A.L. Greer, Confusion by design, Nature 366 (6453) (1993) 303–304.
[9] U. Mizutani, Hume-Rothery rules for structurally complex alloy phases, MRS Bull 37 (2) (2012) 169 169.
[10] A. Inoue, Stabilization of metallic supercooled liquid and bulk amorphous alloys, Acta Mater. 48 (1) (2000) 279–306.
[11] K. Ryan, J. Lengyel, M. Shatruk, Crystal structure prediction via deep learning, J. Am. Chem. Soc. 140 (32) (2018) 10158–10168.
[12] S. Mukherjee, J. Schroers, W.L. Johnson, W.K. Rhim, Influence of kinetic and thermodynamic factors on the glass-forming ability of zirconium-based bulk amorphous alloys, Phys. Rev. Lett. 94 (24) (2005) 245501.
[13] R. Busch, E. Bakke, W.L. Johnson, Viscosity of the supercooled liquid and relaxation at the glass transition of the Zr46.75Ti8.25Cu7.5Ni10Be27.5 bulk metallic glass forming alloy, Acta Mater. 46 (13) (1998) 4725–4732.
[14] O.N. Senkov, Correlation between fragility and glass-forming ability of metallic alloys, Phys. Rev. B 76 (10) (2007) 104202.
[15] W.L. Johnson, J.H. Na, M.D. Demetriou, Quantifying the origin of metallic glass formation, Nat. Commun. 7 (2016) 10313.
[16] D.B. Miracle, A structural model for metallic glasses, Nat. Mater. 3 (10) (2004).
[17] D.B. Miracle, The efficient cluster packing model – an atomic structural model for metallic glasses, Acta Mater 54 (16) (2006) 4317–4336.
[18] Y.F. Ye, C.T. Liu, Y. Yang, A geometric model for intrinsic residual strain and phase stability in high entropy alloys, Acta Mater. 94 (2015) 152–161.
[19] Z.W. Wu, M.Z. Li, W.H. Wang, K.X. Liu, Hidden topological order and its correlation with glass-forming ability in metallic glasses, Nat. Commun. 6 (2015) 6035.
[20] X.J. Liu, Y. Xu, X. Hui, Z.P. Lu, F. Li, G.L. Chen, J. Lu, C.T. Liu, Metallic liquids and glasses: atomic order and global packing, Phys. Rev. Lett. 105 (15) (2010) 155501.
[21] C. Chattopadhyay, K.S.N. Satish Idury, J. Bhatt, K. Mondal, B.S. Murty, Critical evaluation of glass forming ability criteria, Mater. Sci. Technol. 32 (4) (2016) 380–400.
[22] D. Turnbull, Under what conditions can a glass be formed? Contemp. Phys. 10 (5) (1969) 473–488.
[23] A. Inoue, T. Zhang, T. Masumoto, Glass-forming ability of alloys, J. Non-Cryst. Solids 156-158 (1993) 473–480.
[24] Z.P. Lu, C.T. Liu, A new glass-forming ability criterion for bulk metallic glasses, Acta Mater 50 (13) (2002) 3501–3512.
[25] X.H. Du, J.C. Huang, C.T. Liu, Z.P. Lu, New criterion of glass forming ability for bulk metallic glasses, J. Appl. Phys. 101 (8) (2007) 086108.
[26] A.R. Miedema, F.R. de Boer, R. Boom, Model predictions for the enthalpy of formation of transition metal alloys, Calphad 1 (4) (1977) 341–359.
[27] B. Ramakrishna Rao, A.S. Gandhi, S. Vincent, J. Bhatt, B.S. Murty, Prediction of glass forming ability using thermodynamic parameters, Trans. Indian Inst. Metals 65 (6) (2012) 559–563.
[28] G.A. Mansoori, N.F. Carnahan, K.E. Starling, T.W. Leland, Equilibrium thermodynamic properties of the mixture of hard spheres, J. Chem. Phys. 54 (4) (1971) 1523–1525.
[29] S. Fang, X. Xiao, L. Xia, W. Li, Y. Dong, Relationship between the widths of supercooled liquid regions and bond parameters of Mg-based bulk metallic glasses,, J. Non-Cryst. Solids 321 (1) (2003) 120–125.
[30] S. Guo, C.T. Liu, Phase stability in high entropy alloys: Formation of solid–solution phase or amorphous phase, Prog. Nat. Sci.: Mater. Int. 21 (6) (2011) 433–446.
[31] C.A. Angell, Formation of glasses from liquids and biopolymers, Science 267 (5206) (1995) 1924.
[32] L.-M. Wang, Y. Tian, R. Liu, Dependence of glass forming ability on liquid fragility: thermodynamics versus kinetics, Appl. Phys. Lett. 97 (18) (2010) 181901.
[33] J.-P. Correa-Baena, K. Hippalgaonkar, J. van Duren, S. Jaffer, V.R. Chandrasekhar, V. Stevanovic, C. Wadia, S. Guha, T. Buonassisi, Accelerating materials development via automation, machine learning, and high-performance computing, Joule 2 (8) (2018) 1410–1420.
[34] C. Wen, Y. Zhang, C. Wang, D. Xue, Y. Bai, S. Antonov, L. Dai, T. Lookman, Y. Su, Machine learning assisted design of high entropy alloys with desired property, Acta Mater. 170 (2019) 109–117.
[35] R. Ramprasad, R. Batra, G. Pilania, A. Mannodi-Kanakkithodi, C. Kim, Machine learning in materials informatics: recent applications and prospects, NPJ Comput. Mater. 3 (1) (2017) 54.
[36] S. Kuthe, A. Deshmukh, U. Palikundwar, J. Bhatt, Computational platform for manufacturing bulk metallic glasses based on GFA parameters, Trans. Indian Inst. Metals 71 (11) (2018) 2731–2734.
[37] A.-H. Cai, X. Xiong, Y. Liu, W.-k. An, J.-y. Tan, Artificial neural network modeling of reduced glass transition temperature of glass forming alloys, Appl. Phys. Lett. 92 (11) (2008) 111909.
[38] A.-H. Cai, X. Xiong, Y. Liu, W.-k. An, J.-y. Tan, Y. Luo, Artificial neural network modeling for undercooled liquid region of glass forming alloys, Comput. Mater. Sci. 48 (1) (2010) 109–114.
[39] A.H. Cai, Y. Liu, W.K. An, G.J. Zhou, Y. Luo, T.L. Li, X.S. Li, X.F. Tan, Prediction of critical cooling rate for glass forming alloys by artificial neural network, Mater. Des. (1980-2015) 52 (2013) 671–676.
[40] D.R. Cassar, A.C.P.L.F. de Carvalho, E.D. Zanotto, Predicting glass transition temperatures using neural networks, Acta Mater. 159 (2018) 249–256.
[41] Z. Zhou, Y. Zhou, Q. He, Z. Ding, F. Li, Y. Yang, Machine learning guided appraisal and exploration of phase design for high entropy alloys, NPJ Comput. Mater. 5 (1) (2019) 128.
[42] Y.T. Sun, H.Y. Bai, M.Z. Li, W.H. Wang, Machine learning approach for prediction and understanding of glass-forming ability, J. Phys. Chem. Lett. 8 (14) (2017) 3434–3439.
[43] F. Ren, L. Ward, T. Williams, K.J. Laws, C. Wolverton, J. Hattrick-Simpers, A. Mehta, Accelerated discovery of metallic glasses through iteration of machine learning and high-throughput experiments, Sci. Adv. 4 (4) (2018) eaaq1566.
[44] J. Xiong, S.-Q. Shi, T.-Y. Zhang, A machine-learning approach to predicting and understanding the properties of amorphous metallic alloys, Mater. Des. 187 (2020) 108378.
[45] L. Ward, S.C. O'Keeffe, J. Stevick, G.R. Jelbert, M. Aykol, C. Wolverton, A machine learning approach for engineering bulk metallic glass alloys, Acta Mater. 159 (2018) 102–111.
[46] L. Ward, A. Agrawal, A. Choudhary, C. Wolverton, A general-purpose machine learning framework for predicting properties of inorganic materials, NPJ Comput. Mater. 2 (1) (2016) 16028.
[47] J. Xiong, T.-Y. Zhang, S.-Q. Shi, Machine learning prediction of elastic properties and glass-forming ability of bulk metallic glasses, MRS Commun. 9 (2) (2019) 576–585.
[48] Y. Kawazoe, T. Masumoto, K. Suzuki, A. Inoue, A. Tsai, J. Yu, T. Aihara Jr, T. Nakanomyo, Phase Diagrams and Physical Properties of Nonequilibrium Alloys, Springer, Berlin, 1997.
[49] K. Bharath, J.A. Chelvane, M.K. Kumawat, T.K. Nandy, B. Majumdar, Theoretical prediction and experimental evaluation of glass forming ability, density and equilibrium point of Ta based bulk metallic glass alloys, J. Non-Cryst. Solids 512 (2019) 174–183.
[50] W.H. Wang, The elastic properties, elastic models and elastic perspectives of metallic glasses, Prog. Mater. Sci. 57 (3) (2012) 487–656.
[51] A. Takeuchi, A. Inoue, Classification of bulk metallic glasses by atomic size difference, heat of mixing and period of constituent elements and its application to characterization of the main alloying element, Mater. Trans. 46 (12) (2005) 2817–2829.
[52] J.D. Lee, Concise Inorganic Chemistry, John Wiley & Sons, 2008.
[53] Z.Q. Liu, R.F. Wang, R.T. Qu, Z.F. Zhang, Precisely predicting and designing the elasticity of metallic glasses, J. Appl. Phys. 115 (20) (2014) 203513.
[54] W.H. Wang, Correlations between elastic moduli and properties in bulk metallic glasses, J. Appl. Phys. 99 (9) (2006) 093506.
[55] E.S. Park, J.H. Na, D.H. Kim, Correlation between fragility and glass-forming ability/plasticity in metallic glass-forming alloys, Appl. Phys. Lett. 91 (3) (2007) 031907.
[56] K. Mondal, B.S. Murty, On the parameters to assess the glass forming ability of liquids, J. Non-Cryst. Solids 351 (16) (2005) 1366–1371.
[57] X.H. Du, J.C. Huang, New criterion in predicting glass forming ability of various glass-forming systems, Chin. Phys. B 17 (1) (2008) 249–254.
[58] Z. Long, G. Xie, H. Wei, X. Su, J. Peng, P. Zhang, A. Inoue, On the new criterion to assess the glass-forming ability of metallic alloys, Mater. Sci. Eng., A 509 (1) (2009) 23–30.
[59] D.E. Rumelhart, G.E. Hinton, R.J. Williams, Learning representations by back--propagating errors, Nature 323 (6088) (1986) 533–536.
[60] A. Suliman, Y. Zhang, A review on back-propagation neural networks in the application of remote sensing image classification, J. Earth Sci. Eng. 5 (2005) 52–65.
[61] Z.P. Lu, C.T. Liu, Y.D. Dong, Effects of atomic bonding nature and size mismatch on thermal stability and glass-forming ability of bulk metallic glasses, J. Non-Cryst. Solids 341 (1) (2004) 93–100.
[62] C.S. Ma, J. Zhang, X.C. Chang, W.L. Hou, J.Q. Wang, Electronegativity difference as a factor for evaluating the thermal stability of Al-rich metallic glasses, Philos. Mag. Lett. 88 (12) (2008) 917–924.
[63] E. Alcobaça, S.M. Mastelini, T. Botari, B.A. Pimentel, D.R. Cassar, A.C.P. de Leon Ferreira de Carvalho, E.D Zanotto, Explainable machine learning algorithms for predicting glass transition temperatures, Acta Mater 188 (2020) 92–100.
[64] G. Kim, H. Diao, C. Lee, A.T. Samaei, T. Phan, M. de Jong, K. An, D. Ma, P.K. Liaw, W. Chen, First-principles and machine learning predictions of elasticity in severely lattice-distorted high-entropy alloys with experimental validation, Acta Mater. 181 (2019) 124–138.